


RESEARCH ARTICLE

Estimating B_1^+ in the breast at 7T using a generic templateMichael J. van Rijssel  | Josien P. W. Pluim | Peter R. Luijten | Kenneth G. A. Gilhuijs | Alexander W. J. Raaijmakers | Dennis W. J. KlompCenter for Image Sciences, UMC Utrecht,
Utrecht, The Netherlands**Correspondence**Mike van Rijssel, University Medical Center
Utrecht, Heidelberglaan 100, Room Q.02.4.45,
3584 CX Utrecht, The Netherlands.
Email: mrijsse2@umcutrecht.nl**Funding information**

ZonMw, Grant/Award Number: 104003019

Dynamic contrast-enhanced MRI is the workhorse of breast MRI, where the diagnosis of lesions is largely based on the enhancement curve shape. However, this curve shape is biased by RF transmit (B_1^+) field inhomogeneities. B_1^+ field information is required in order to correct these. The use of a generic, coil-specific B_1^+ template is proposed and tested.

Finite-difference time-domain simulations for B_1^+ were performed for healthy female volunteers with a wide range of breast anatomies. A generic B_1^+ template was constructed by averaging simulations based on four volunteers. Three-dimensional B_1^+ maps were acquired in 15 other volunteers. Root mean square error (RMSE) metrics were calculated between individual simulations and the template, and between individual measurements and the template. The agreement between the proposed template approach and a B_1^+ mapping method was compared against the agreement between acquisition and reacquisition using the same mapping protocol.

RMSE values (% of nominal flip angle) comparing individual simulations with the template were in the range 2.00–4.01%, with mean 2.68%. RMSE values comparing individual measurements with the template were in the range 8.1–16%, with mean 11.7%. The agreement between the proposed template approach and a B_1^+ mapping method was only slightly worse than the agreement between two consecutive acquisitions using the same mapping protocol in one volunteer: the range of agreement increased from $\pm 16\%$ of the nominal angle for repeated measurement to $\pm 22\%$ for the B_1^+ template.

With local RF transmit coils, intersubject differences in B_1^+ fields of the breast are comparable to the accuracy of B_1^+ mapping methods, even at 7 T. Consequently, a single generic B_1^+ template suits subjects over a wide range of breast anatomies, eliminating the need for a time-consuming B_1^+ mapping protocol.

KEYWORDS7 T, B_1^+ mapping, breast, flip-angle correction, RF field, T_1 mapping**1 | INTRODUCTION**

Dynamic contrast-enhanced MRI (DCE-MRI) is the workhorse of clinical breast MRI examinations. Since its introduction in the 1980s, it has become a standard in breast MRI examinations due to its robustness and ability to detect tumor malignancy.^{1,2} This ability is based on the differences in dynamics of contrast agent uptake between tumors and healthy parenchymal tissue, leading to characteristic enhancement curve shapes. Automated analysis of these curves enabled the introduction of computer aided diagnosis methods into clinical practice, and pharmacokinetic models have been proposed to quantify the exchange of contrast agents between the inflowing blood and surrounding tissue.^{3–5}

Abbreviations used: B_1^+ , RF transmit field; DCE-MRI, dynamic contrast-enhanced MRI; DESPOT1, driven-equilibrium single-pulse observation of T_1 ; DREAM, dual refocusing echo acquisition mode; RMSE, root mean square error; SAR, specific absorption rate; SD, standard deviation; T_1 NR, T_1 -to-noise ratio.

This is an open access article under the terms of the Creative Commons Attribution License, which permits use, distribution and reproduction in any medium, provided the original work is properly cited.

© 2018 The Authors. *NMR in Biomedicine* published by John Wiley & Sons Ltd.

Taking breast DCE-MRI to higher field strengths such as 7 T is currently being investigated, showing potential for earlier and more accurate diagnosis.⁶ The higher signal-to-noise ratio that is available at higher field strengths enables higher spatial resolution. A higher resolution not only permits detection of smaller lesions, but also improves assessment of the heterogeneity of contrast uptake, such as rim enhancement, which is associated with worse survival in triple negative breast cancers.⁷ It was shown that using the available signal-to-noise ratio to achieve a higher temporal resolution at 7 T is also feasible in a clinical setting.⁸

A fast wash-out rate is a typical indication of a malignant tumor, while a stable curve or continued wash-in often reflects benign lesions. However, the curve shape can be compromised by RF transmit (B_1^+) field variations, potentially shifting the curve of a tumor that should have caused a wash-out shape into a more stable curve. This can be conceptually understood by considering the fact that at different B_1^+ levels there are different amounts of T_1 saturation, and the effects of a change in T_1 (due to contrast administration) will differ. If we define B_1^+ induced image

$$\text{intensity bias as } \frac{\text{measured intensity}}{\text{true intensity } (B_1^+ = 100\%)}, \text{ then for fast RF spoiled gradient echo sequences bias} = \frac{\sin(B_1^+ \theta_{\text{nom}}) \left(1 - e^{-T_R/T_1} \cos(\theta_{\text{nom}})\right)}{\sin(\theta_{\text{nom}}) \left(1 - e^{-T_R/T_1} \cos(B_1^+ \theta_{\text{nom}})\right)}. \text{ Observe}$$

that this bias depends not only on B_1^+ , but also on T_1 , which in DCE-MRI is not constant in time, and the image intensity bias will change over the dynamic series. Generally, for any B_1^+ below 100%, the bias increases with increasing T_1 ; consequently, when the T_1 of tumor tissue drops due to contrast injection, the DCE curve's wash-in is reduced due to the counteracting effect of the intensity bias. The opposite effect occurs when due to contrast wash-out the tumor's T_1 rises again, leading to a compromised curve, shifted to appear more stable than the true curve.

Correction for this B_1^+ effect is possible, using B_1^+ field maps and an estimate of T_1 before contrast injection.⁹ It has been shown that applying B_1^+ correction at 3 T has a significant effect on the results of quantitative analysis and serves to reduce differences in quantitative parameter estimations between the right and left breasts.¹⁰ Recent work shows that, even at 1.5 T, refraining from B_1^+ field corrections leads to a 50% estimation error in tumor T_1 and consequently a 41% estimation error in pharmacokinetic parameters.¹¹ At 7 T, the B_1^+ field variations manifest themselves on a smaller spatial scale, such that variations within a single breast become significant. Therefore, when applying DCE-MRI at 7 T, corrections using B_1^+ field maps are imperative.

B_1^+ field variations are much more significant at higher field strengths due to the reduced wavelength of the RF field. At 7 T, the proton excitation frequency is 300 MHz, leading to an RF wavelength of around 15 cm inside the body (assuming a relative permittivity around 60). The breasts, however, contain high amounts of fat, which has a relative permittivity that is an order of magnitude lower than that of most other tissues. This leads to a longer RF wavelength inside the breasts, approximately 40 cm assuming a relative permittivity around 10. Such a wavelength is usually larger than the size of the imaged anatomy. In this case, the B_1^+ field distribution within the breast will depend mainly on the local transmit setup used, and hardly at all on the individual anatomy. Therefore, we hypothesize that one generic, coil-specific B_1^+ template will suit a wide range of subjects in the case of breast examinations with local transmit coils. We set out to test our hypothesis at 7 T, where local transmit is a commonly used strategy to overcome RF inhomogeneity issues.

The advantages of using a generic B_1^+ template in a clinical setting are twofold. It eliminates the need to acquire a B_1^+ field map, saving scan time. Furthermore, B_1^+ mapping techniques are known to be prone to noise and many are only reliable within a certain range.^{12,13} Since the generic template is based on (partly simulated) data of multiple subjects, it is essentially noise free and reliable in the full range of B_1^+ inhomogeneities present. Though other techniques to estimate B_1^+ in breast without acquiring field maps exist, these methods often rely on fat as a reference tissue (with a fixed T_1) in order to estimate B_1^+ in the parenchyma.^{14,15} Such methods may not be suitable for fat-suppressed sequences and rely on extrapolation of a fitted field distribution outside fatty regions. The template method presented is not hampered by these limitations, since B_1^+ distributions can be deducted regardless of the sequence used. This method is limited only by the availability of a B_1^+ template of the coil design used.

The present work aims to explore the feasibility of using a generic B_1^+ template by investigating the inter-subject differences in B_1^+ inhomogeneity. The work comprises both simulated field maps and measured ones, in order to compare template performance with the accuracy of B_1^+ mapping.

2 | METHODS

In order to test our hypothesis that one generic, coil-specific B_1^+ template will suit a wide range of subjects when performing breast MRI with local transmit coils, a number of experiments were performed. First, RF simulations from previous work were used to create the template (Section 2.1). Next, B_1^+ and T_1 mapping was performed on 15 new volunteers (Section 2.2) and their breast volume and composition were estimated (Section 2.3). Section 2.4 describes Q measurements of the coil that we conducted to investigate the influence of breast anatomy on coil loading. The acquired B_1^+ maps were used to compare against the predictions made using the constructed template (Section 2.5). Finally, we tested the ability of the B_1^+ template predictions to correct T_1 maps for B_1^+ inhomogeneity corruption against B_1^+ map corrected T_1 measurements (Section 2.6), using methodology that is common in quantitative DCE-MRI.

All experiments conducted were in accordance with the guidelines of the local ethical committee and, prior to the examination, written informed consent was obtained from all volunteers.

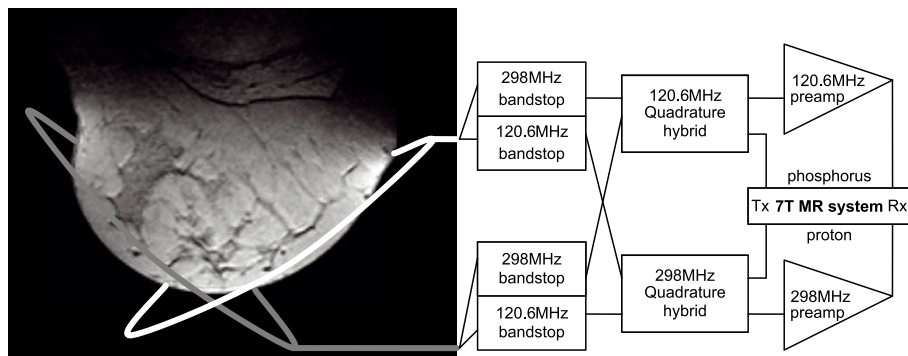


FIGURE 1 Schematic overview of the dual-channel unilateral breast coil for the detection of ^{31}P and ^1H MR signals. The locations of the two elements are illustrated by two ellipsoids on a transverse MR image of the human breast. These elements are interfaced to the transmit (Tx) and receive (Rx) line of the 7 T MR system using bandstop filters, quadrature hybrids and preamplifiers as illustrated on the right. Reproduced from Reference 16

2.1 | Simulations and template construction

The coil setup used in this work was a quadrature setup as illustrated in Figure 1 and presented in earlier work by Klomp et al.¹⁶ Their work also demonstrates the high efficiency of this coil and its usefulness in imaging and spectroscopy applications for 7 T breast MRI.

Finite-difference time-domain simulations of B_1^+ and B_1^- distributions in five healthy female volunteers (V1-V5), presented in previous work, were used to investigate inter-subject differences in B_1^+ distribution at 7 T when using this local transmit coil setup.¹⁷ In short, B_1 field distributions were calculated from personalized breast segmentations obtained from T1w Dixon scans fused with Virtual Family model Ella, and a 3D model of the relevant MR equipment.^{18,19} Segmentations of glandular tissue, adipose tissue and skin were assigned their corresponding dielectric permittivity and conductivity values.²⁰ Finite-difference time-domain simulations were conducted for 201 000 time steps of 3×10^{-12} s (one Larmor period) with a mesh of $2 \times 2 \times 2$ mm³, assuming perfectly absorbing boundary layers. Convergence was assessed by visual inspection. Coil losses were not considered, since these have no impact on B_1^+ distributions. Vitamin tablets were attached to the coil elements using adhesive tape, in order to identify their position in the T1w scans. Though a limited number of volunteers were used to conduct the simulations, volunteers were selected to represent a reasonably wide range in breast anatomies, as can be appreciated from their T1w gradient echo scans in Figure 2 and anatomical characteristics in Table 1. Due to missing data, the simulation for V1 had to be excluded.

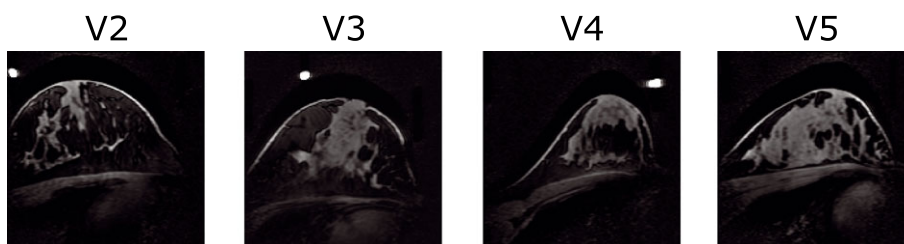


FIGURE 2 Fat-suppressed T₁w scans of the four included simulation volunteers (sagittal view). Bright dots mark the locations of vitamin tablets used to determine the position of the coil by van der Velden et al.¹⁷

TABLE 1 Inclusion table reporting the breast volume and volumetric glandular percentage for all simulation volunteers (V2-V5)

Number	Breast volume (cm ³)	Gland percentage
V2	756	17%
V3	777	29%
V4	285	33%
V5	474	44%
Mean	573	31%
SD	205	9%
Min.	285	17%
Max.	777	44%

In order to directly compare the simulated B_1^+ and B_1^- fields, which did not share a common coordinate system, all simulated field distributions were aligned using multi-resolution intensity-based rigid registration in elastix.²¹ For this purpose, a mutual information similarity metric, third-order B-spline interpolation and an adaptive stochastic gradient descent optimizer were used. This allows transmit coil alignment, since these coils are present in the simulations as hyperintense fields closest to the coil conductors. Differences in RF amplification settings between volunteers were overcome by normalizing all simulations relative to the simulation of V5 (arbitrarily chosen). In order to do so, the following intensity scaling factor was applied to the simulated field distribution for volunteers V2-V5:

$$\text{scale}(i) = \text{median} \left\{ \forall \vec{r}: \frac{\text{simulation}_5(\vec{r})}{\text{simulation}_i(\vec{r})} \right\}$$

where i is the volunteer number and $\vec{r} = (x, y, z)$ the position in the simulation. Note that the median was preferred over the mean to ensure robustness against outliers.

Subsequently, the average of the rescaled simulation distributions of volunteer V2-V5 was taken, we denote these the B_1^+ and B_1^- templates. Differences between volunteers were assessed per volunteer by comparing each individual simulation result with the B_1^+ template. The comparison was quantified using mean difference, standard deviation (SD) of difference and root mean square error (RMSE) metrics. All metrics were calculated over all voxels within the breast region of interest, which was determined previously.¹⁷ The B_1^- template was created to facilitate B_1^+ template scaling using information obtained from the power optimization phase.

2.2 | Scanning protocol

In order to prospectively compare the accuracy of the template approach with B_1^+ mapping, a validation set of 15 additional healthy female volunteers (S1-S15), mean age 39 years (range 24-62, all ages are reported in Table 2), were scanned in the prone position using the same unilateral breast coil setup on a 7 T whole-body MR system (Achieva; Philips, Cleveland, OH, USA).¹⁶ A 3D B_1^+ map was acquired using the dual refocusing echo acquisition mode (DREAM) technique with the following parameters: pulse repetition time 4.0 ms, stimulated echo time 1.49 ms, free induction decay echo time 1.97 ms, 2.5 mm isotropic resolution, preparation angle 55°, imaging angle 25° and turbo field echo factor 32.¹² For three volunteers, S13-S15, the DREAM B_1^+ acquisition was repeated, to compare the accuracy of the proposed template method with the variation between repeated measures. 3D T_1 -weighted gradient echo images were acquired at four flip angles (2°, 4°, 13° and 27°) using Dixon water-fat separation with the following parameters: in-phase echo time 1.97 ms, out-phase echo time 4.4 ms, repetition time 6.0 ms and isotropic resolution 1.5 mm.¹⁹ Both scans were planned according to a fast survey scan; measurements obtained during this scan's power optimization phase were

TABLE 2 Inclusion table reporting the age, breast volume, volumetric glandular percentage and ratio $Q_{\text{unloaded}}/Q_{\text{loaded}}$ for all validation volunteers (S1-S15)

Number	Age (years)	Breast volume (cm ³)	Gland percentage	$Q_{\text{unloaded}}/Q_{\text{loaded}}$
S1	24	495	28%	–
S2	26	479	28%	3.2
S3	24	638	64%	5.2
S4	25	382	26%	3.7
S5	30	309	25%	3.7
S6	33	213	38%	3.9
S7	57	184	17%	3.0
S8	62	570	10%	–
S9	45	1032	7.2%	–
S10	55	235	24%	2.8
S11	53	928	7.5%	4.5
S12	40	707	41%	–
S13	28	129	87%	–
S14	24	351	81%	–
S15	28	494	35%	–
Mean	36.9	476	35%	3.7
SD	13.4	256	25%	0.74
Min.	24	129	7.2%	2.8
Max.	62	1032	87%	5.2

TABLE 3 Summary of scan parameters per sequence

Sequence	T_R (ms)	T_E (ms)	Resolution (mm ³)	Flip angle (°)	Other parameters
DREAM B_1^+ mapping	4	SE: 1.49FID: 1.97	$2.5 \times 2.5 \times 2.5$	Preparation: 55Imaging: 25	TFE acceleration factor: 32
Dual-echo gradient echo (4x)	6	IP: 1.97OP: 4.4	$1.5 \times 1.5 \times 1.5$	2/4/13/27	Dixon reconstruction: water & fat images
Survey (3D, fast RF spoiled gradient echo)	6	1.25	$3 \times 3 \times 10$	10	Reconstructed to $2 \times 2 \times 5$ mm ³

logged and later used in template scaling. Scan parameters for both sequences are summarized in Table 3. The B_1^+ map and variable flip angle images allowed the calculation of T_1 maps using the driven-equilibrium single-pulse observation of T_1 relaxation (DESPO1) technique²²; see the T_1 mapping section for more details and the rationale behind the choice of angles.

2.3 | Estimating breast volume and composition

Estimates of breast volume and composition were calculated for all volunteers. Since the pectoral muscle was not visible for all volunteers due to the limited range where the coil transmits and receives sufficient signal, estimates of breast volume were obtained using the method described by Katariya et al.²³ on transversal maximum intensity projections. Though this method is rather simplistic and potentially imprecise, it has been shown to be highly reproducible and correlated with mastectomy excision volume, and allows for comparison with published population data.^{24,25} The Dixon water and fat reconstructions were used to estimate volumetric gland percentage for each volunteer.

2.4 | Q-factor measurements

In order to check individual differences of coil loading, all volunteers (S1-S15) were asked to return on a different day for additional Q-factor measurements. Out of 15, nine volunteers were able to participate but in one volunteer the measurement failed, leading to eight useable data points. Measurements were made using a purpose-built coil that contained a replica of the innermost element of the coil that was used in the MR experiments. The mechanics of the setup were identical to those used in the scanner. The Q factor (defined as central resonance frequency over bandwidth) was determined using a network analyzer. Volunteers were asked to lie down in the prone position on the setup as they did in the scanner, positioning the arms on their back. Values for Q both with and without loading were recorded for each volunteer; the ratio $Q_{\text{unloaded}}/Q_{\text{loaded}}$ was calculated as a measure for coil loading. The ratios were plotted against breast volume and volumetric glandular percentage for each volunteer, and a trend line was calculated using analytical ordinary least squares estimation.

2.5 | Comparing B_1^+ template and measured maps

Rigid registration was applied to the B_1^+ template to facilitate direct comparison with the measured B_1^+ map for every volunteer. The map was masked before registration to exclude regions where a B_1^+ reconstruction was not available. The template was masked by thresholding to exclude values corresponding to flip angles below 20% and above 100% of the nominal flip angle. All values higher than 100% are very close to or in coil elements; the bottom cut-off of 20% was empirically chosen to avoid registration of the edge of the map to the edge of the template. In the resulting binary image, a 3D connected components algorithm using a 6-connected neighborhood was used to find connected regions. The largest connected component was selected as the mask. Multi-resolution intensity-based rigid registration was applied in elastix, using a mutual information similarity metric, B-spline interpolation and an adaptive stochastic gradient descent optimizer.

Subsequently, the B_1^+ values of the registered template were intensity scaled using information from the scanner's power optimization phase. During this phase, a global B_1^+ level (PO B_1^+) for the sample is measured. Using scanner log data from the power optimization phase for all volunteers, a calibration line was determined between this global PO B_1^+ and an average B_1^+ value determined from the registered template, scaled to match the measured B_1^+ map (i.e. the best possible template scale for every volunteer). Taking into account the global nature of the PO B_1^+ , the

average B_1^+ value was weighted with both B_1^+ and B_1^- : $\text{weighted}|B_1^+| = \frac{\sum_{r \in M} ((B_1^-(r)B_1^+(r))B_1^+(r))}{\sum_{r \in M} (B_1^-(r)B_1^+(r))}$, where M is a mask created by thresholding the

survey scan using Otsu's method.²⁶ The calibration line obtained in this fashion was subsequently used to scale each registered B_1^+ template, independently of its measured B_1^+ map.

The map and the registered template were compared on individual bases through calculation of the RMSE, mean error and SD of the error per volunteer and a total mean absolute error for the validation set. Additionally, a Bland-Altman density plot was created, showing the agreement between the measured B_1^+ map and the registered and scaled template for all 15 volunteers (S1-S15). As suggested by Bland and Altman, the same kind of plot was created for two repeated DREAM-based B_1^+ mapping measurements to study repeatability.²⁷ This allowed for comparison of the

limits of agreement between the template method and the DREAM method with the degree of variation between repeated B_1^+ mapping procedures for volunteers S13-S15.

2.6 | T_1 mapping

As is commonly done in quantitative DCE-MRI, we used B_1^+ maps to correct for the effects of B_1^+ inhomogeneities using a variable flip-angle T_1 mapping method.^{10,11,22,28,29} This method uses several T_1 -weighted gradient echo scans at different flip angles to estimate the T_1 value at every recorded voxel by performing a fit of the signal equation, which is a function of the applied flip angle. Since this is a voxel-wise method, B_1^+ correction can be easily applied by fitting the function while using the actual flip angle as the independent variable, i.e. the nominal angle multiplied by the value in the B_1^+ map for that voxel.

The flip-angle combination was chosen by taking into consideration the notions put forth by Deoni et al.,³⁰ ensuring an accurate T_1 measurement over the wide B_1^+ range (50-120% of the nominal angle) and the wide T_1 range (600-2200 ms) present in the breast. To determine the best flip-angle combination, all combinations of four integer angles in the range 1-90° were tested and the T_1 -to-noise ratio (T_1 NR) was calculated for every combination of angles with T_1 set to either 600 or 2200 ms and B_1^+ set to either 50% or 120% of the nominal angle. The sum over all four combinations of B_1^+ and T_1 for T_1 NR determined the suitability of every combination of angles. Figure 3 shows the T_1 NR using the selected flip angle combination (2°, 4°, 13° and 27°) over a wide range of T_1 values for three levels of B_1^+ .

T_1 maps were calculated from the data using the DESPOT1 method.²² In the fitting procedure, the independent variable was either the nominal angle, the angle as measured by the DREAM sequence or the angle as predicted by the template. This leads to T_1 maps that are not corrected for B_1^+ , corrected by the DREAM B_1^+ data or corrected by the generic B_1^+ template respectively. The SD of the T_1 estimate was calculated in every voxel, following the methodology described in Reference 30. An estimate of the noise level was obtained by taking the SD of the image intensity in anatomy-free regions of the gradient echo images. Finally, all voxels for which the SD in the T_1 estimate was larger than 100 ms were (empirically) considered unreliable and excluded (the average exclusion percentage was 10.3% of all voxels inside the region where the DREAM B_1^+ map was defined).

The obtained T_1 maps were analyzed by comparing the measurements corrected using the measured map versus using the template. The T_1 estimates were compared on individual bases through calculation of the RMSE, mean error and SD of the error.

3 | RESULTS

Table 1 shows the breast volume and volumetric glandular percentage of all simulation volunteers; Table 2 shows the same for all validation volunteers. In the simulation set, breast volume ranged from 285 to 777 cm³ and glandular percentage from 17 to 44%; in the validation set, breast volume ranged from 129 to 1032 cm³ and glandular percentage from 7 to 87%.

The difference between the constructed generic template and every individual volunteer's simulation is shown in Figure 4. Panel B shows that the differences between individuals are small particularly compared with the large dynamic range in B_1^+ in each individual. As Table 4 shows, the mean RMSE between the generic template and individual simulations was 2.68% of the nominal angle, while in the worst agreeing volunteer (V2) this was 4.01%.

Measurements for $Q_{\text{unloaded}}/Q_{\text{loaded}}$ ranged from 2.8 to 5.2. Measurements per volunteer are reported in Table 2.

The calibration line used in power-optimization-based scaling of the template is shown in Figure 5. The calibration line fit had an adjusted R^2 of 0.825. The (registered and scaled) generic template and the measured B_1^+ map are similar, as can be appreciated visually from Figure 6. It shows both the best matching case (S6) and the worst matching case (S11), based on the RMSE. Table 5 shows statistics for all volunteers (S1-S15).

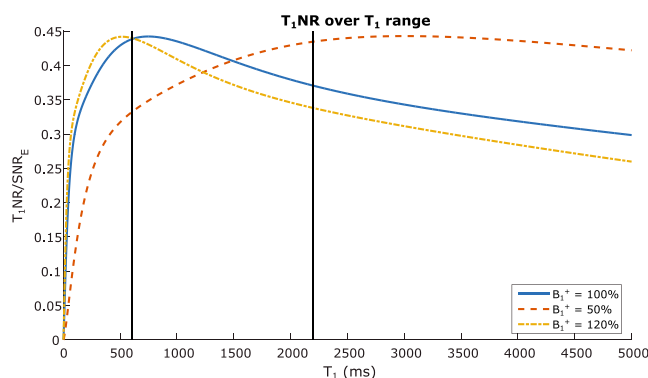


FIGURE 3 T_1 NR of the variable-flip-angle acquisition scheme, when using the DESPOT1 analysis method. Profiles for T_1 -to-noise are plotted for three levels of B_1^+ ; vertical lines indicate the T_1 values for glandular tissue (2200 ms) and fat (600 ms)

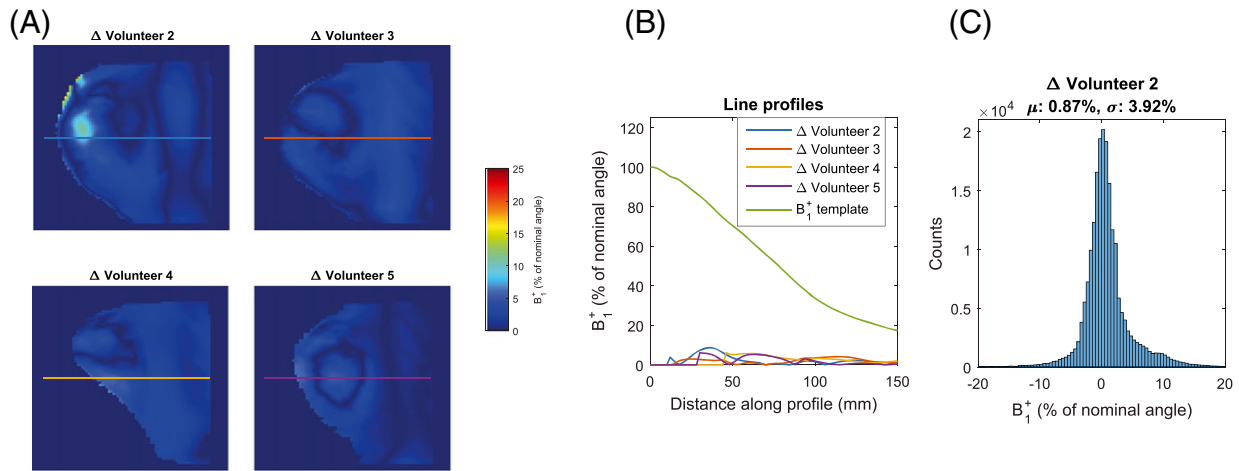


FIGURE 4 A, Absolute difference between mean B_1^+ (template) and individual simulations. B, Line profiles corresponding to same-colored lines in A. C, Histogram of difference between template and simulation of Volunteer 2 (which showed least agreement)

TABLE 4 Comparison between individual B_1^+ simulations and the generic template for all simulation volunteers (V2-V5)

Number	Mean error (% of nom. angle)	SD of error (% ona)	RMSE (% ona)
V2	0.87	3.92	4.01
V3	0.80	2.24	2.38
V4	-1.42	1.85	2.34
V5	0.35	1.97	2.00
Mean	0.15	2.50	2.68
SD	0.93	0.83	0.78
Min.	-1.42	1.85	2.00
Max.	0.87	3.92	4.01

% ona, percentage of nominal angle.

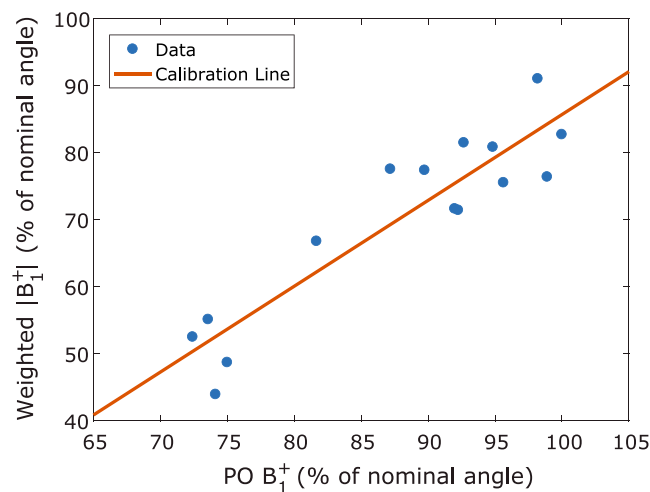


FIGURE 5 Calibration line for B_1^+ template scaling. The global B_1^+ measured during the scanner's power optimization phase is regressed against a weighted average of the B_1^+ template, scaled to match the measured B_1^+ map. Adjusted R^2 of the fit is 0.825

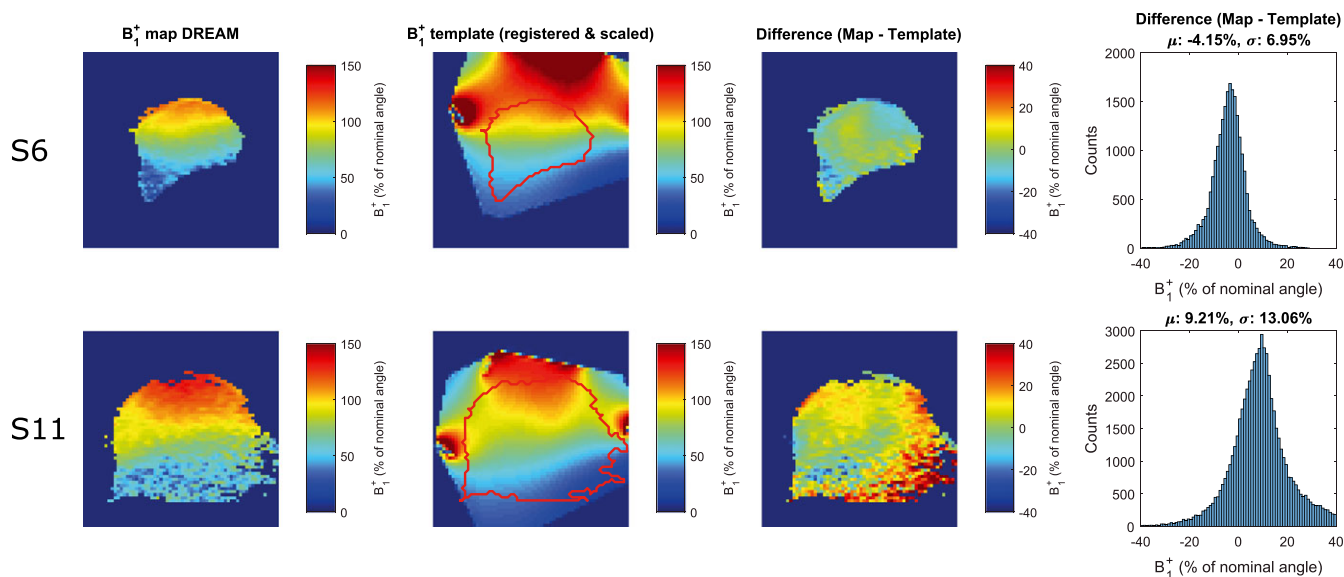


FIGURE 6 For volunteer S6 (top row) and volunteer S11 (bottom row), from left to right: B_1^+ map measured with DREAM technique; B_1^+ template registered and scaled to measured map (the red line indicates the breast outline as in the first panel); difference between template and map; histogram of difference between template and map

TABLE 5 Comparison between individual B_1^+ measurements and the generic template for all validation volunteers (S1-S15)

	Mean error (% of nom. angle)	SD of error (% ona)	RMSE (% ona)
S1	-1.9	11	11
S2	7.9	9.4	12
S3	-0.93	12	12
S4	4.9	8.3	9.6
S5	3.9	7.5	8.4
S6	-4.2	7.0	8.1
S7	-6.3	8.4	10
S8	3.0	10	10
S9	5.6	12	14
S10	2.2	9.0	9.3
S11	9.2	13	16
S12	8.8	12	15
S13	-10	11	15
S14	-5.5	11	13
S15	-6.1	11	12
Mean	0.710	10.2	11.7
SD	5.96	1.85	2.34
Min.	-10	7.0	8.1
Max.	9.2	13	16

% ona, percentage of nominal angle.

The mean RMSE between the generic template and individual prospective measurements was 11.7% of the nominal angle; the total mean absolute error was 5.37%. The Bland-Altman analysis of all volunteers in Figure 7A shows that the measured maps and generic template agree less in regions with low B_1^+ than areas with high B_1^+ . Figure 7B shows the same analysis for a subset; only data from volunteers S13-S15 has been included. Figure 7C shows a Bland-Altman analysis of repeated DREAM B_1^+ mapping for the same volunteers (S13-S15); note that the limits of agreement are 12% wider in B than in C.

T_1 estimates calculated with DESPOT1 and either map-based or template-based B_1^+ information are close, as can be appreciated visually in Figure 8 for Volunteer S1. Table 6 shows a quantitative analysis for all volunteers (S1-S15); the mean RMSE was 318 ms.

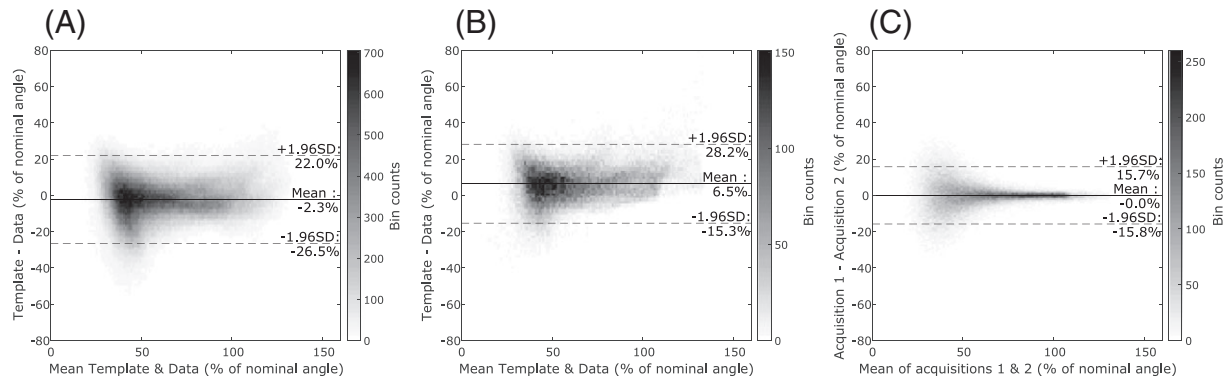


FIGURE 7 A, Bland-Altman analysis of the registered templates and measured maps for all volunteers (S1-S15). The data is visualized using a density histogram; the scale bar on the right indicates the amount of counts in each bin. B, Bland-Altman analysis of a subset of the data displayed in A; only volunteers S13-S15 are shown. C, Bland-Altman analysis of repeatedly measured B_1^+ maps of volunteers S13-S15

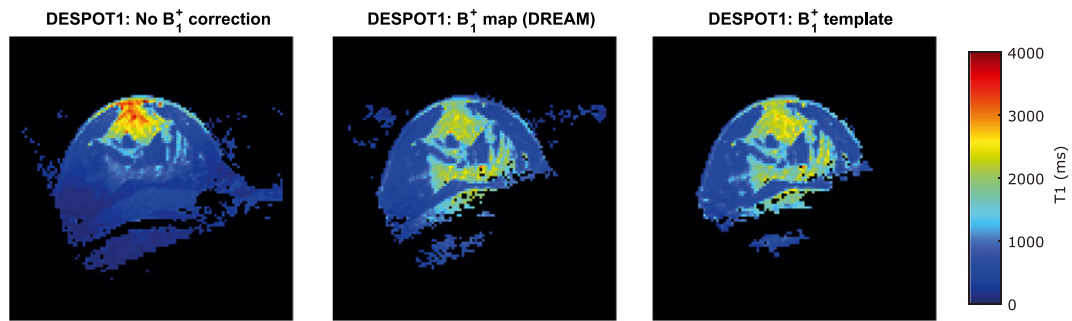


FIGURE 8 For volunteer S1, from left to right: T_1 map using DESPOT1 and no B_1^+ correction; T_1 map using DESPOT1 and B_1^+ map measured with DREAM; T_1 map using DESPOT1 and B_1^+ template registered and scaled to measured map

TABLE 6 Comparison between the DREAM-corrected and template-corrected measurements of T_1 (ms) for all validation volunteers (S1-S15)

	Mean error (ms)	SD of error (ms)	RMSE (ms)
S1	-54	171	180
S2	213	255	332
S3	-80	231	244
S4	160	215	268
S5	146	295	329
S6	-144	201	248
S7	-232	261	349
S8	-47	225	230
S9	-66	184	196
S10	-23	286	287
S11	-110	165	199
S12	-181	353	397
S13	-586	359	687
S14	300	400	500
S15	187	272	331
Mean	-34	258	318
SD	213	68	128
Min.	-586	165	180
Max.	300	400	687

4 | DISCUSSION

Our results from the simulations show that differences in B_1^+ distributions in the breast between volunteers covering a wide anatomical range are generally very small, only of the order of 2-3%. This amount of variation is of the same order of magnitude as the accuracy of popular B_1^+ mapping methods.³¹ This is a strong indication that, in breast MRI with local RF transmit coils at 7 T or lower, resorting to field mapping for every subject is unnecessary.

The width of the anatomical range of the validation set, quantified in Table 2, is substantial, in terms of both breast volume and glandular percentage. Comparing our distribution of breast volumes to that of 225 healthy women in Reference 24 shows that we have captured a wide range, except for the high end of the spectrum, since the maximum included volume is only 1 SD away from the reported average; sadly, our coil setup and non-wide-bore MR system are incapable of accommodating women with higher breast volumes. The included range of breast densities is also broad when compared with a representative group of 531 consecutively included patients receiving breast MRI; the largest reported volumetric glandular percentage is 50% in Reference 32. Note that Gubern-Mérida et al. showed that volumetric estimations of breast density based on MRI tend to underestimate BI-RADS (Breast Imaging Reporting and Data System) density scores, and in their study of 132 women from a high-risk group with age characteristics comparable to those in our study none of the subjects had a percentage higher than 60%.³³ The width of the simulation set is inevitably smaller, due to the small number of four volunteers included. Yet it captures a reasonably wide range (at least 1 SD from the average for both breast density and volume) and, arguably, our results obtained with only the limited simulation set only make the case for a template-based B_1^+ estimation stronger.

Our results from the measured B_1^+ maps show that a generic template can accommodate volunteers over a wide range of breast anatomies. The Bland-Altman analysis in Figure 7A makes it clear that the measured maps are interchangeable with the registered and scaled generic template, within the range between the limits of agreement (-26.5% to $+22.0\%$ of the nominal angle). In other words, if one is satisfied with an error between the two methods up to approximately 20% of the nominal angle, the methods may be exchanged. Note that the range of agreement is considerably narrower (and thus better) if one were to exclude regions where B_1^+ is low, where the measured maps are unreliable.¹² In those regions, the generic template might actually be at an advantage, since it does not suffer from such a limitation and is noise-free in nature. To investigate whether the observed limits of agreement between the proposed template method and the DREAM method are acceptable, Figures 7B and 6C show the results for three volunteers (S13-S15) of an identical Bland-Altman analysis between measured data and proposed template (6B) and between measured data and repeated measurement (6C). The range between the limits of agreement is slightly larger for the template than for repeated measurements: where repeated measurements had an error of up to 15% of the nominal angle for volunteers S13-S15, this range increased by approximately 6% using a B_1^+ template. The bias that can be observed in Figure 7B is mainly due to the use of the calibration line for template scaling, and this bias will differ for each volunteer. Note from Table 5 that volunteers S13-S15 all have quite large mean errors, which explains the high mean offset (bias) in Figure 7B; for most subjects, this bias will be smaller.

It is clear from Figure 8 that the B_1^+ corrected DESPOT1-based T_1 maps are substantially more homogeneous in both lipids and glandular tissue, irrespective of whether the B_1^+ information is from a map or the template. When comparing the analyses in Table 5 and Table 6 it is clear that the mean errors in B_1^+ propagate into mean errors in T_1 estimates. In all cases but one, the SD of the error distribution is bigger than the mean error, which means that the two measurements of T_1 do not significantly differ.

A limitation of this study is the fact that we have to rely on RF simulations to be able to construct the template. Several studies, however, have shown that these kinds of simulation are able to accurately predict B_1^+ distributions and show high agreement between measured and simulated field maps.³⁴⁻³⁷ The fact that all simulations were performed using a single body model with different breast models may further impact the validity of our simulations, though since local transmit coils were used the effect will be limited to an increase or decrease of the total efficiency. If this effect is present, it will be corrected by the intensity scaling of the registered template (Section 2.4). The results of the Q measurements also contribute to this conclusion. While they show that tissue load is dominant ($Q_{\text{unloaded}}/Q_{\text{loaded}}$ was around 4 for all volunteers), they also show that, even with breast volume changes by up to a factor of 5, load variations were all within 30% of $Q_{\text{unloaded}}/Q_{\text{loaded}} = 4$. This means that the biggest tissue load is caused by the rest of the body and that the Q variance over breast anatomies is limited, analogous to our results in B_1^+ . Probably the RF eddy currents that occur in the rest of the body predominantly have a local B_1^+ effect that is either of insufficient strength to affect the B_1^+ in the breast, or hardly differs from the effects observed in the Virtual Family model (Ella).

Though this paper only demonstrates the use of a template for a unilateral breast coil, we believe that this can be extended to bilateral cases. Hardware developments in high-field MRI tend to go towards parallel multi-transmit systems, where amplitude and phase of all coil elements can be steered individually. In such setups, regarding each breast independently in terms of B_1^+ is a reasonable assumption.

It is of note that demonstrating agreement between measured and simulated B_1^+ distributions is often used to validate predictions in specific absorption rate (SAR). While our work shows that B_1^+ distributions in the breast are very similar from person to person, the same does not necessarily hold for SAR. In fact, in recent work by Alon et al., it was demonstrated that B_1^+ distributions tend to be correlated over samples, but the same did not hold for SAR.³⁸ Therefore, they conclude that using B_1^+ distributions to validate SAR predictions should be done with caution. The present work serves as further proof of the statement that B_1^+ distributions tend to have high correlations between subjects; this is the very phenomenon we exploit when constructing and using a B_1^+ template.

Implementation of the generic template approach in a clinical setting requires knowledge of both the position of the transmit coil in the image and the amount of template scaling that is needed for each subject. In many setups, the position of the coil is fixed on the bed, eliminating

the positioning problem altogether. We have solved the scaling issue by using readily available information from the power optimization phase and the survey scan, information that will be present in any clinical protocol. This strategy brings a dependence of the template's performance on the goodness of fit of the calibration line of Figure 5: a large variation from the calibration line causes a large mean error (bias) in the resulting template-based B_1^+ distribution. As reported in Table 5, the SD of the mean error was 5.96% of the nominal angle; in the ideal situation where the scaling is calculated directly from a measured B_1^+ map, this SD reduces to 1.78% of the nominal angle. The main reason for the reduced performance (and the goodness of fit of the calibration line) might be that the B_1^+ measured during the power optimization procedure is non-localized. Therefore, it was assumed that the measured B_1^+ level during the power optimization was a weighted average over the entire imaged region that contained tissue. The differences in mean error between volunteers may be further reduced when a localized power optimization method is employed for template scaling.³⁹

In conclusion, simulations show that inter-subject differences in B_1^+ fields of the breast at 7 T are comparable to the accuracy of popular B_1^+ mapping methods reported in literature. Consequently, we have shown that, at the cost of a small loss in accuracy (the range of agreement increased from $\pm 16\%$ of the nominal angle for repeated measurement to $\pm 22\%$ for the B_1^+ template), using a generic B_1^+ template to account for substantial RF transmit inhomogeneity in T_1 mapping may be feasible across a wide range of volunteers.

ORCID

Michael J. van Rijssel  <http://orcid.org/0000-0002-2365-4408>

REFERENCES

- Kaiser WA, Zeitler E. MR imaging of the breast—fast imaging sequences with and without Gd-DTPA—preliminary observations. *Radiology*. 1989;170(3):681-686.
- Morris EA. Breast cancer imaging with MRI. *Radiol Clin North Am*. 2002;40(3):443-466.
- Chen WJ, Giger ML, Bick U, Newstead GM. Automatic identification and classification of characteristic kinetic curves of breast lesions on DCE-MRI. *Med Phys*. 2006;33(8):2878-2887.
- Gilhuijs KGA, Giger ML, Bick U. Computerized analysis of breast lesions in three dimensions using dynamic magnetic-resonance imaging. *Med Phys*. 1998;25(9):1647-1654.
- Tofts PS, Berkowitz B, Schnall MD. Quantitative-analysis of dynamic Gd-DTPA enhancement in breast-tumors using a permeability model. *Magn Reson Med*. 1995;33(4):564-568.
- Stehouwer BL, Klomp DWJ, van den Bosch MAAJ, et al. Dynamic contrast-enhanced and ultra-high-resolution breast MRI at 7.0 Tesla. *Eur Radiol*. 2013;23(11):2961-2968.
- Schmitz AMT, Loo CE, Wesseling J, Pijnappel RM, Gilhuijs KGA. Association between rim enhancement of breast cancer on dynamic contrast-enhanced MRI and patient outcome: impact of subtype. *Breast Cancer Res Treat*. 2014;148(3):541-551.
- Pinker K, Bogner W, Baltzer P, et al. Clinical application of bilateral high temporal and spatial resolution dynamic contrast-enhanced magnetic resonance imaging of the breast at 7 T. *Eur Radiol*. 2014;24(4):913-920.
- Haacke EM, Filletti CL, Gattu R, et al. New algorithm for quantifying vascular changes in dynamic contrast-enhanced MRI independent of absolute T_1 values. *Magn Reson Med*. 2007;58(3):463-472.
- Bedair R, Graves MJ, Patterson AJ, et al. Effect of radiofrequency transmit field correction on quantitative dynamic contrast-enhanced MR imaging of the breast at 3.0 T. *Radiology*. 2016;279(2):368-377.
- Tsai W-C, Kao K-J, Chang K-M, et al. B_1 field correction of T_1 estimation should be considered for breast dynamic contrast-enhanced MR imaging even at 1.5 T. *Radiology*. 2017;282(1):55-62.
- Nehrke K, Börner P. DREAM—a novel approach for robust, ultrafast, multislice B_1 mapping. *Magn Reson Med*. 2012;68(5):1517-1526.
- Yarnykh VL. Actual flip-angle imaging in the pulsed steady state: a method for rapid three-dimensional mapping of the transmitted radiofrequency field. *Magn Reson Med*. 2007;57(1):192-200.
- Pineda FD, Medved M, Fan XB, Karczmar GS. B_1 and T_1 mapping of the breast with a reference tissue method. *Magn Reson Med*. 2016;75(4):1565-1573.
- Sung K, Saranathan M, Daniel BL, Hargreaves BA. Simultaneous T_1 and B_1^+ mapping using reference region variable flip angle imaging. *Magn Reson Med*. 2013;70(4):954-961.
- Klomp DWJ, van de Bank BL, Raaijmakers A, et al. ^{31}P MRSI and ^1H MRS at 7T: initial results in human breast cancer. *NMR Biomed*. 2011;24(10):1337-1342.
- van der Velden TA, Italiaander M, van der Kemp WJM, et al. Radiofrequency configuration to facilitate bilateral breast ^{31}P MR spectroscopic imaging and high-resolution MRI at 7 Tesla. *Magn Reson Med*. 2015;74(6):1803-1810.
- Christ A, Kainz W, Hahn EG, et al. The Virtual Family—development of surface-based anatomical models of two adults and two children for dosimetric simulations. *Phys Med Biol*. 2010;55(2):N23-N38.
- Dixon WT. Simple proton spectroscopic imaging. *Radiology*. 1984;153(1):189-194.
- Gabriel C, Gabriel S, Corthout E. The dielectric properties of biological tissues. 1. Literature survey. *Phys Med Biol*. 1996;41(11):2231-2249.
- Klein S, Staring M, Murphy K, Viergever MA, Pluim JPW. elastix: a toolbox for intensity-based medical image registration. *IEEE Trans Med Imaging*. 2010;29(1):196-205.
- Deoni SCL, Rutt BK, Peters TM. Rapid combined T_1 and T_2 mapping using gradient recalled acquisition in the steady state. *Magn Reson Med*. 2003;49(3):515-526.
- Katariya RN, Forrest APM, Gravelle IH. Breast volumes in cancer of breast. *Br J Cancer*. 1974;29(3):270-273.

24. Scutt D, Manning JT, Whitehouse GH, Leinster SJ, Massey CP. The relationship between breast asymmetry, breast size and the occurrence of breast cancer. *Br J Radiol.* 1997;70(838):1017-1021.
25. Senie RT, Rosen PP, Lesser ML, Snyder RE, Schottenfeld D, Duthie K. Epidemiology of breast-carcinoma II: factors related to the predominance of left-sided disease. *Cancer.* 1980;46(7):1705-1713.
26. Otsu N. A threshold selection method from gray-level histograms. *IEEE Trans Syst Man Cybernet.* 1979;9(1):62-66.
27. Bland JM, Altman DG. Statistical methods for assessing agreement between two methods of clinical measurement. *Lancet.* 1986;1(8476):307-310.
28. Christensen KA, Grant DM, Schulman EM, Walling C. Optimal determination of relaxation-times of Fourier-transform nuclear magnetic-resonance—determination of spin-lattice relaxation-times in chemically polarized species. *J Phys Chem.* 1974;78(19):1971-1977.
29. Homer J, Beevers MS. Driven-equilibrium single-pulse observation of T_1 relaxation—a reevaluation of a rapid new method for determining NMR spin-lattice relaxation-times. *J Magn Reson.* 1985;63(2):287-297.
30. Deoni SCL, Peters TM, Rutt BK. Determination of optimal angles for variable nutation proton magnetic spin-lattice, T_1 , and spin-spin, T_2 , relaxation times measurement. *Magn Reson Med.* 2004;51(1):194-199.
31. Nehrke K, Sprinkart AM, Börrner P. An in vivo comparison of the DREAM sequence with current RF shim technology. *Magn Reson Mater Phys Biol Med.* 2015;28(2):185-194.
32. van der Velden BHM, Dmitriev I, Loo CE, Pijnappel RM, Gilhuijs KGA. Association between parenchymal enhancement of the contralateral breast in dynamic contrast-enhanced MR imaging and outcome of patients with unilateral invasive breast cancer. *Radiology.* 2015;276(3):675-685.
33. Gubern-Mérida A, Kallenberg M, Platel B, Mann RM, Marti R, Karssemeijer N. Volumetric breast density estimation from full-field digital mammograms: a validation study. *PLoS ONE.* 2014;9(1):e85952. <https://doi.org/10.1371/journal.pone.0085952>
34. Graesslin I, Homann H, Biederer S, et al. A specific absorption rate prediction concept for parallel transmission MR. *Magn Reson Med.* 2012;68(5):1664-1674.
35. Homann H, Bornert P, Eggers H, Nehrke K, Dossel O, Graesslin I. Toward individualized SAR models and in vivo validation. *Magn Reson Med.* 2011;66(6):1767-1776.
36. Murbach M, Neufeld E, Capstick M, et al. Thermal tissue damage model analyzed for different whole-body SAR and scan durations for standard MR body coils. *Magn Reson Med.* 2014;71(1):421-431.
37. Voigt T, Homann H, Katscher U, Doessel O. Patient-individual local SAR determination: in vivo measurements and numerical validation. *Magn Reson Med.* 2012;68(4):1117-1126.
38. Alon L, Deniz CM, Carluccio G, Brown R, Sodickson DK, Collins CM. Effects of anatomical differences on electromagnetic fields, SAR, and temperature change. *Concepts Magn Reson B.* 2016;46(1):8-18.
39. Versluis MJ, Kan HE, van Buchem MA, Webb AG. Improved signal to noise in proton spectroscopy of the human calf muscle at 7 T using localized B_1 calibration. *Magn Reson Med.* 2010;63(1):207-211.

How to cite this article: van Rijssel MJ, Pluim JPW, Luijten PR, Gilhuijs KGA, Raaijmakers AWJ, Klomp DWJ. Estimating B_1^+ in the breast at 7 T using a generic template. *NMR in Biomedicine.* 2018;e3911. <https://doi.org/10.1002/nbm.3911>